



Contents lists available at ScienceDirect

Tectonophysics

journal homepage: [www.elsevier.com/locate/tecto](http://www.elsevier.com/locate/tecto)

## Fault modelling of the early-2014 ~M6 Earthquakes in Cephalonia Island (W. Greece) based on GPS measurements

Vassilis Sakkas\*, Evangelos Lagios

Department of Geophysics & Geothermics, Remote Sensing Laboratory, University of Athens, Panepistimiopolis-Illissia, Athens 157 84, Greece

### ARTICLE INFO

#### Article history:

Received 3 August 2014

Received in revised form 20 January 2015

Accepted 21 January 2015

Available online xxx

#### Keywords:

Fault modelling

Ground deformation

GPS measurements

Cephalonia Island

Ionian Sea

### ABSTRACT

Modelling of ground deformation was performed based on GPS measurements that were collected in the western part of Cephalonia (Paliki Peninsula) which had experienced two moderate magnitude earthquakes in early 2014. Both events of magnitudes  $M_w = 6.1$  (Jan. 26) and  $M_w = 5.9$  (Feb. 3) had the same right-lateral character of motion with a small thrust component, but different focal depth of 16 km and 5 km, respectively. The GPS results show large amplitudes of displacement in both horizontal (6–40 cm) and vertical (8–15 cm) components in the vicinity of Paliki for the period 2010–2014, which is attributed primarily to those earthquakes. Various scenarios of activated faults were considered to model the observed ground deformation that was associated with those events. The most plausible case that accounts for a realistic and best-fit approximation of the measured displacement vectors has a solution of two activated faults of SSW–NNE trending direction that are separated by a small offset. Consistent with the lack of surface exposure of the seismogenic faults, the best-fit model assumes two easterly dipping fault planes at burial depths of 0.8 km and 0.5 km and at angles of 72° and 65°, respectively. The GPS deduced models clearly resolved the plane ambiguities associated with the focal mechanism solutions of the two major events. A small “normal-fault” component along the upper part of the fault planes should be considered to further improve the best-fit approximation of the observed vertical deformation. It was also found that a non-negligible deformational component from aftershocks is inherent in the observed data mainly from Paliki.

© 2015 Elsevier B.V. All rights reserved.

### 1. Introduction

The region of the central Ionian Sea (Greece) is tectonically very active. It plays an important role in the kinematic processes of the broader area, as it constitutes part of the Eastern Mediterranean lithosphere that is subducting beneath the Aegean lithosphere along the Hellenic Arc. It lies within a seismotectonically active region that is undergoing rapid and intense ground deformation (Ganas et al., 2013; Lagios et al., 2007, 2012; Reilinger et al., 2010). The subduction zone terminates against a major strike–slip fault, the Cephalonia Transform Fault (CTF) that is located just offshore of Paliki Peninsula (Fig. 1). Cephalonia Island comprises the western part of the fold-belt of the external Hellenides. It mainly consists of Alpine Mesozoic and Cenozoic sedimentary rocks, the Paxos or Pre-Apulia zone and the overthrust Ionian zone. The Pre-Apulia zone forms the major part of Cephalonia. The Ionian zone is dominated by compressional tectonics. The boundary of the zone is defined by the Ionian thrust. This thrust is well exposed in Cephalonia where a distinct scarp has formed with Mesozoic carbonates of the hanging wall lying next to eroded Miocene marls. A more detailed

description of the tectonic regime may be found in our previous works (Lagios et al., 2007, 2012).

The highest seismic activity in Europe currently takes place in the Ionian region. Very strong earthquakes and associated intense co- and post-seismic ground motions have taken place in the past, such as the August 1953 catastrophic earthquake sequence that devastated not only Cephalonia but also the neighbouring islands of Ithaca and Zakynthos (Galanopoulos, 1962; Stiros et al., 1994). The high seismicity in the central Ionian Sea is the result of intense crustal deformation associated with right-lateral strike–slip faulting along the CTF which supports earthquakes of magnitudes up to  $M_w = 7.4$  (Louvari et al., 1999). Several large-magnitude earthquakes have occurred in the vicinity. Some of the most recent large-magnitude events include: (1) January 17, 1983 ( $M_w = 6.7$ ) in Cephalonia, (2) August 14, 2003 ( $M_w = 6.3$ ) to the west of Lefkas (e.g. Papadimitriou et al., 2006; Pavlides et al., 2004), and (3) a sequence of earthquakes in October 2005 ( $M_w = 5.6$ ) and April 2006 ( $M_w = 5.5$ – $5.7$ ) to the south of Zakynthos (Papadimitriou et al., 2012). Since then, no other events of comparable magnitudes have occurred until January 2014.

In early 2014, a sequence of three seismic events of magnitudes  $M_w = 6.1$  (January 26; 13:55 UTC),  $M_w = 5.2$  (January 26; 18:45 UTC) and  $M_w = 5.9$  (February 3; 03:08 UTC) took place underneath the island

\* Corresponding author. Tel.: +30 2107274914; fax: +30 2107274787.  
E-mail address: [vsakkas@geol.uoa.gr](mailto:vsakkas@geol.uoa.gr) (V. Sakkas).

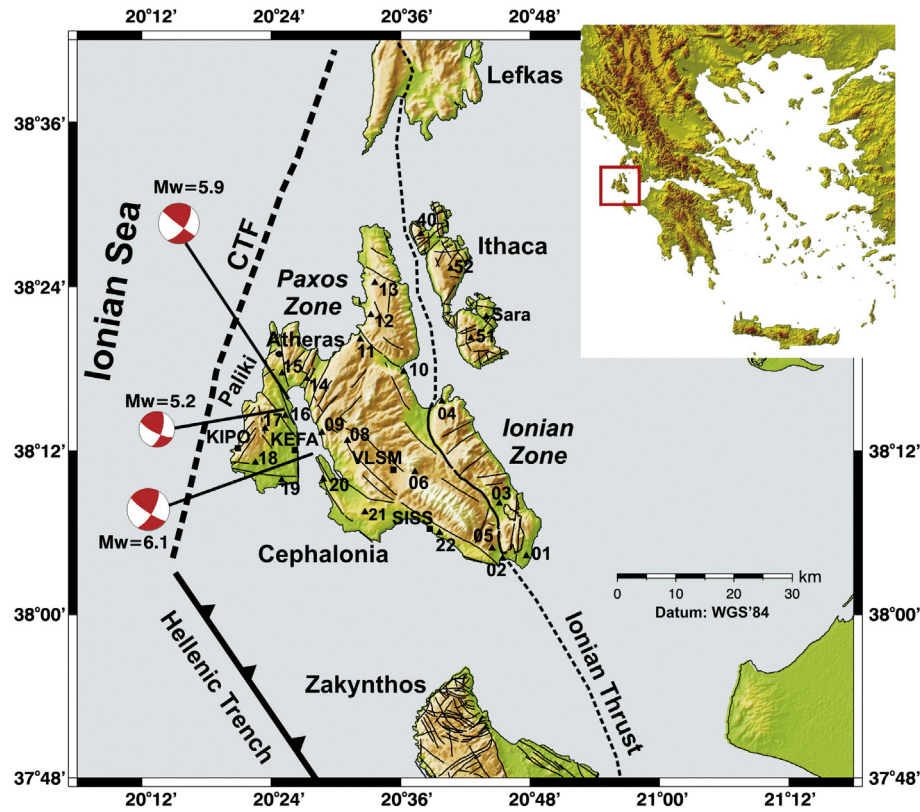


**Fig. 1.** GPS station network in Cephalonia & Ithaca islands. Rectangles and triangles represent continuous and campaign GPS stations, respectively, showing also the Cephalonia Transform Fault (CTF), the approximate boundary (broken line) between the Ionian and Paxos Zone, together with the focal mechanisms of the early-2014 earthquake sequence. Station cGPS KEFA is located at Lyxouri.

of Cephalonia (Karakostas et al., 2014; Papadimitriou et al., 2014; Papadopoulos et al., 2014). These events induced extensive structural damages and geo-environmental effects mainly in the western part of the island at Paliki Peninsula (see Fig. 2 and Table 1). Following the outbreak of the sequence, intense post-seismic activity involving hundreds of aftershocks with magnitudes ( $M_w$ ) between 2 and 4.5 had occurred over the ensuing months.

This paper reports on the observed deformational pattern associated with the aforementioned recent earthquakes as measured by periodic reoccupations of a GPS network that had been initially installed in Cephalonia in 2001 (Lagios et al., 2007). In addition, the presumed activation of faults has been considered in an effort to model the observed ground deformation by taking into consideration the recent sequence of earthquakes.

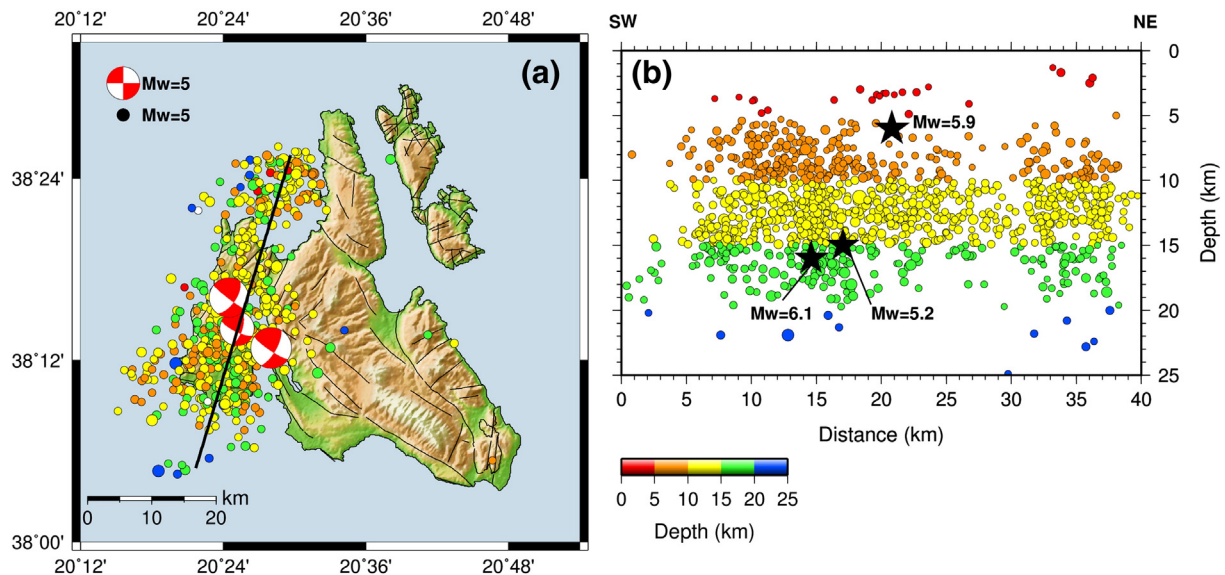


**Fig. 2.** (a) Distribution of earthquake epicenters for the period January to April 2014 ( $M_w > 3$ ), including the focal mechanism solutions of the three major events of early 2014. (b) Cross-section of the earthquake hypocenters along the SW-NE trending line (a). Earthquake epicenters were taken from Geodynamic Institute, National Observatory of Athens (NOA), Greece.

**Table 1**  
Focal mechanism parameters of early-2014 ~M6 earthquakes in Cephalonia.

	Mw = 6.1	Mw = 5.9	Mw = 5.2
Date	January 26th, 2014	February 2nd, 2014	January 26th, 2014
Time (UTC)	13:55:42	03:08:44	18:45:07
Latitude (°N)	38.2133	38.2689	38.2349
Longitude (°E)	20.4772	20.4081	20.4194
Depth (km)	16.0	5.0	15.0
Strike (degrees)	30	35	18
Dip (degrees)	70	62	65
Rake (degrees)	169	175	162
Seismic moment (dyn-cm)	2.03E+25	9.60E+24	8.34E+23

Source: Department of Geophysics & Geothermics, University of Athens, Greece.

## 2. The GPS measurements

A GPS network consisting of 27 stations (benchmarks) was installed on Cephalonia Island in 2001 and expanded to Ithaca Island in 2004 (Fig. 1) to study the kinematics among the recognized fault-blocks of these islands. This network was remeasured several times (Lagios et al., 2007), and subsequently the results of two recent campaigns (2007 and 2010) were combined with analysis of available Permanent Scatterer Interferometric (PSI) data (Lagios et al., 2012).

After the early-2014 earthquake sequence, the network was remeasured in late February to early March 2014, after the occurrence of the second major event. Data from continuous GPS (cGPS) recording stations were also processed and included in the present analysis. Time series for the period January 1st to May 5th 2014 were compiled from three cGPS stations: (i) Valsamata (VLSM), (ii) Kipouria (KIPO) (both stations being operated by the Geodynamic Institute of the National Observatory of Athens, Greece), and (iii) Sissia (SISS) which is our station that was established in March 2014 (Fig. 3). The benchmarks were occupied using Leica receivers of types SR399, SR9500 and GRX1200. For each daily session, the occupied stations were tied-up to VLSM that served as a local reference station. The motion of VLSM is well known (Lagios et al., 2012), as it has been operated since 2005. Each roving station was occupied at least twice at a sampling rate of 15 s, and a nominal duration time of about 48–56 h for each occupational period.

The Bernese Software version 5.2 (Dach et al., 2007) was used for the long-term analysis of all GPS data. Horizontal and vertical displacements were estimated with respect to IGB08 reference frame (<http://igsceb.jpl.nasa.gov/network/refframe.html>). The recorded data at KIPO, SISS, and VLSM were tied up and processed using the observational data from a number of IGS (International GNSS Service) Reference Frame Stations in Europe (<http://www.epncb.oma.be>); namely, AUT1, DUTH & DYNG (Greece), GRAZ (Austria), MATE & USAL (Italy), GRAS (France), GSR1 (Slovenia), SOFI (Bulgaria) and WTZR (Germany). Precise orbits, Earth orientation parameters (EOP), satellite clock corrections and GPS monthly P1-C1 code bias solutions were obtained from the CODE analysis centre (<ftp://ftp.unibe.ch/aiub/CODE>); grids for the Vienna Mapping Function (<http://ggsatm.hg.tuwien.ac.at>), atmospheric (<http://geophy.uni.lu/>) and ocean (<http://holt.oso.chalmers.se/loading>) tidal loading coefficients were used to calculate a set of high precision station coordinates. The long-time span of the data significantly reduced uncertainties (at a 90% confidence level) for the majority of the stations to overall rms errors of about 1.8–7.8 mm and 2.7–11.0 mm for the horizontal and vertical displacements, respectively.

The variation of the absolute coordinates (IGB08) for station VLSM is depicted graphically in Fig. 3a. Until the occurrence of the seismic events, this station exhibited the anticipated regional motion of the area with respect to IGB08 (Hollenstein et al., 2008), that is a NNE horizontal motion with velocities of  $V_{East} = 17.8 \pm 0.2$  mm/yr,  $V_{North} = 3.5 \pm 0.4$  mm/yr and  $V_{Up} = 1.3 \pm 1.1$  mm/yr (Lagios et al., 2012). However, the seismic events of January 26th (1st event) and February 3rd (2nd event) 2014 caused a severe WSW subsidence with respect to

IGB08. The overall directional movement for the period 2010–2014 is ENE ( $\approx 85^\circ$  CW to N), with amplitudes of  $39.4 \pm 3.7$  mm and  $-11.8 \pm 3.1$  mm for the horizontal and vertical displacements, respectively. The accumulated co-seismic deformation for the two events is  $28 \pm 3.1$  mm in a WSW horizontal direction ( $\approx 244.5^\circ$  CW to N) and  $-11.4 \pm 2.9$  mm in the vertical component. It is noted that the two events caused an almost identical type of co-seismic motion in both horizontal ( $\Delta_h$ ) and vertical ( $\Delta_v$ ) components ( $\Delta_{h1st} = 14.1 \pm 1.8$  mm &  $\Delta_{h2nd} = 13.9 \pm 2.1$  mm and  $\Delta_{v1st} = -5.5 \pm 2.8$  mm &  $\Delta_{v2nd} = -5.9 \pm 2.7$  mm). A nearby benchmark to VLSM, station 06 which served as a local reference station from 2001 to 2010, also showed a similar motion (Fig. 3b) but with a more intense subsidence of  $-31.8 \pm 2.7$  mm, and horizontal displacement of  $47.5 \pm 2.9$  mm (direction  $\approx 80^\circ$  CW to N) for the period 2010–2014. Also note that the time series from station KIPO are also shown (Fig. 3a). It is evident that daily solutions do not show a consistent stability, since limited recording data were available. Finally, a set of steady daily solutions from the station SISS was possible to be extracted.

Data for all GPS campaigns were tied up to station VLSM, which itself was tied to the IGB08 reference frame. Therefore, all calculated station-coordinates are with respect to the IGB08 reference frame.

### 2.1. The GPS results

Fig. 4 represents the displacement vectors of the GPS network for the period 2010–2014 (Table I, Supplementary Section) with respect to IGB08 reference frame. It is apparent that the observed deformation should include pre-, co- and aftershock effects, as well as the regional motion of the area with respect to IGB08 for the time span of about four years (2010–2014). In order to determine the deformation ( $u_d$ ) due to the seismic sequence in early 2014, the measured position in 2014 ( $p_1$ ) was taken into consideration together with the estimated position ( $p_{est}$ ) of each GPS station before the occurrence of the seismic activity:

$$u_d = p_1 - p_{est}, \text{ and } p_{est} = p_0 + v \cdot t$$

where  $p_0$  is the position in 2010,  $v$  is the estimated velocities of the stations (Lagios et al., 2012), and  $t$  is the time-lapse between the occurrence of the first event of the seismic sequence and the prior measurement of the GPS network in 2010 (i.e.,  $t = 3.9$  years).

The estimated displacement errors,  $\sigma_d$ , were determined by taking into consideration the velocity errors ( $\sigma_v$ ) and the positional errors ( $\sigma_0$  and  $\sigma_1$ ) for 2010 and 2014 (Protti et al., 2014):

$$\sigma_d = \sqrt{\sigma_0^2 + \sigma_1^2 + (\sigma_v \cdot t)^2}.$$

These errors were on average calculated to be 8.6% for the horizontal component and 10.1% for the vertical component of the displacement magnitudes. It was determined that the errors were greater than the estimated deformational magnitudes especially for the stations located at the south-eastern part of the island, away from the activated zone.

Fig. 5 shows the estimated co- and post-deformations due to the early-2014 seismic sequence (Table II, Supplementary Section). The vector for the station KIPO was calculated from data only for the period September 2013 to February 2014, since the station was not in continuous operation. Final results for the station KEFA operating at Lyxouri area, which were published by the National Technical University of Athens (Greece)—(<http://147.102.110.73/src/kefallonia.htm>), were also incorporated.

The most prominent deformation for the period 2010–2014 is the large amplitudes for the horizontal displacement in the area of Paliki (Fig. 4a), where the intense seismic activity occurred. Strong differential displacements with horizontal components reaching amplitudes of 40 cm indicate the faulting zone that generated the seismic activity. At

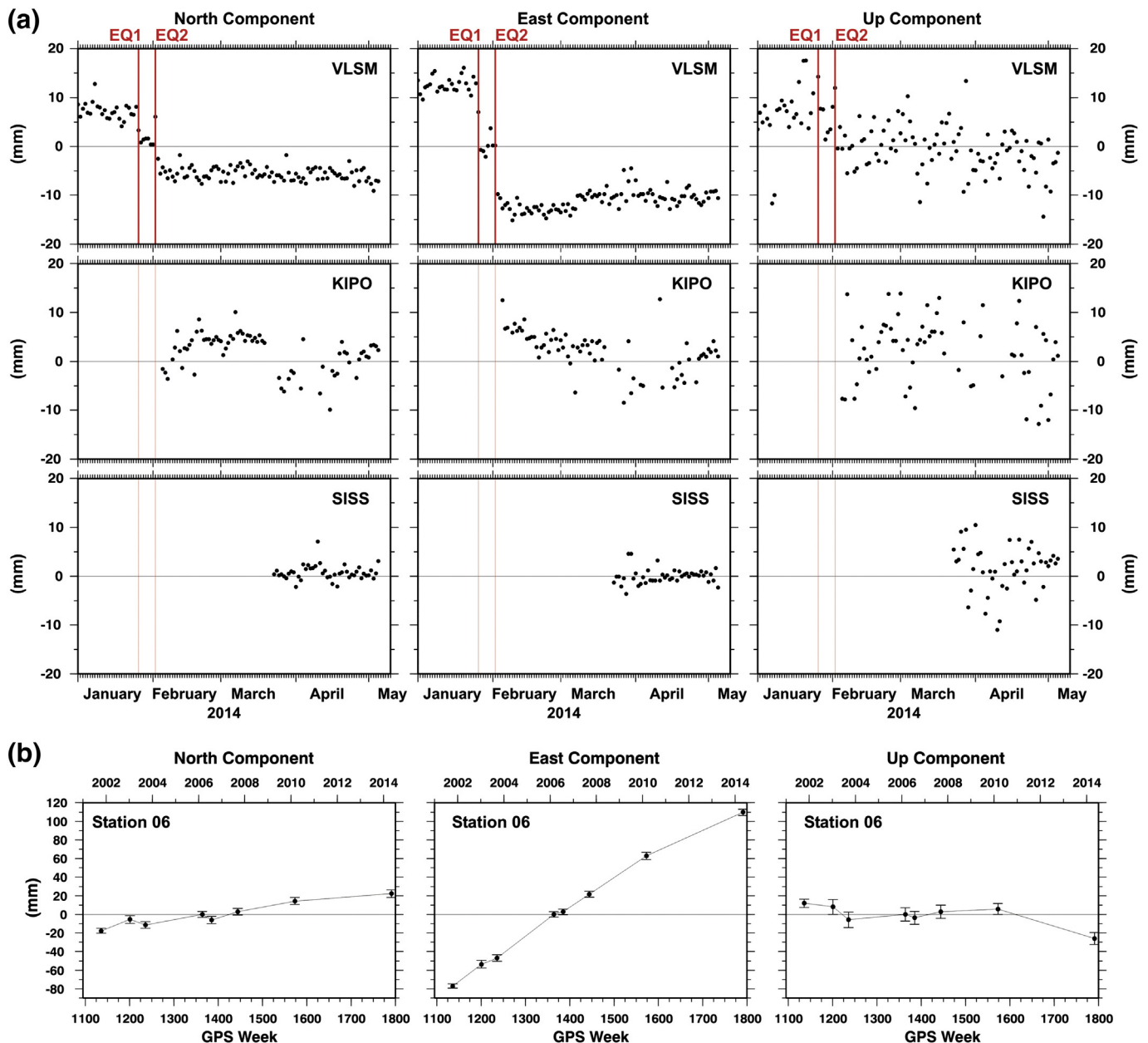


Fig. 3. (a) Time series of cGPS stations (VLSM, KIPO, SISS) for the period January 1st to May 5th, 2014; (b) variation of coordinates for station 06 (period 2001–2014) (Reference Frame: IGB08).

the southern part of Paliki, stations located at its south-eastern part moved in a SSE direction with a mean amplitude of about 16 cm, while the stations further to the west exhibited a northward displacement with increased amplitude (from about 6 cm at station 18 to about 16 cm at station 17). The differences in movements between stations 16 and 14, indicating NE and SW motions, respectively, underline the differential motions across Paliki and the rest of the island. Finally, station 15 which is close to the Atheras Village at the northern part shows the strongest observed horizontal displacement at about 40 cm in a NNW direction.

The overall direction and amplitude of the displacement vectors in Paliki are indicative of the characteristics (location, probable limits and direction) of the seismogenic faults in this area. However, a closer inspection of the horizontal component shows that station 16, although being located almost in the centre of the activated area, has an amplitude that is significantly smaller ( $\approx 9$  cm) as compared to other stations (14, 15, 17) in the vicinity. Considering the change of motion at

station 15 together with the  $M_w = 5.2$  event that occurred close to station 16, a discontinuity or a kinematic boundary may be present that counterbalanced the anticipated motion at this station. Lastly, the large horizontal displacement (up to 40 cm) at station 15 is not so easily related to the significantly smaller displacements for the rest of the neighbouring stations. However, a more detailed discussion for this station (No 15) is presented below.

The vertical component of displacement (Fig. 4b) reveals a significant uplift (up to 15 cm) along Paliki, while subsidence is observed at the stations in the vicinity to the east of the peninsula. This latter observation emphasizes the differential character of the deformation that has occurred over the region. The strongest subsidence is observed at station 14 (about 11 cm) and marks the transition from the main island to the peninsula. However, it is noted that the stations on Paliki exhibit also a differential character along its length with amplitude of uplift decreasing from North to South (15 cm at station 15 to 8 cm at KEFA), as well as from East to West (13 cm at station 16 to 5 cm at KIPO).

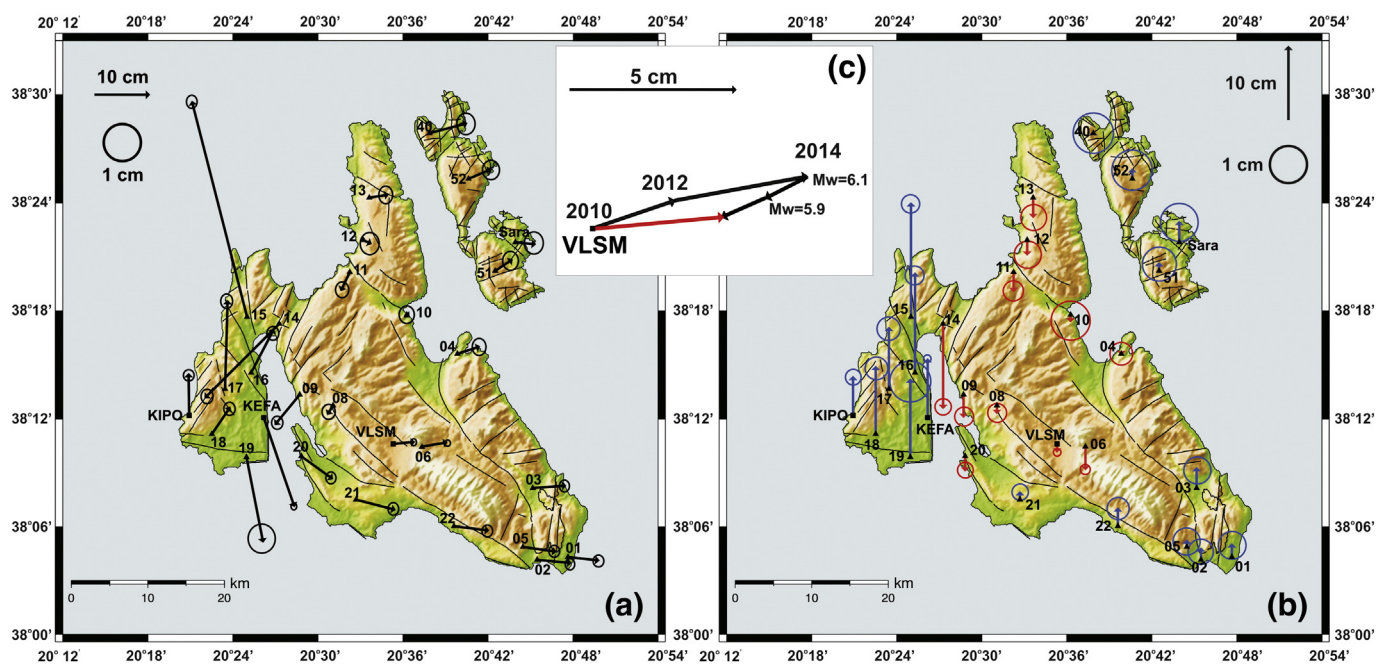


**Fig. 4.** (a) Horizontal, and (b) vertical displacements of GPS stations for the period 2010–2014 (time lapse  $\sim 3.9$  years). Red and blue arrows indicate subsidence and uplift, respectively. (c) Horizontal motion of cGPS station VLSM for the period 2010–2014, showing the co-seismic motion during the two major events (Reference Frame: IGB08). (For interpretation of the references to colour in this figure legend, the reader is referred to the web version of this article.)

The ground deformations on the central and southeastern part of Cephalonia and Ithaca reveal a more uniform pattern of significantly smaller amplitudes, which is consistent with the expected tectonic motions of the islands and the regional motion of the broader area (Lagios et al., 2012). The main discrepancies emerge at stations that are located close to the seismically affected area in Cephalonia (08, 09, 11 & 20). Stations 09 and 08 show SW displacements that are almost parallel to station 14 but with decreasing amplitude moving eastwards from the epicentral area,  $\approx 7$  cm and  $\approx 2$  cm, respectively. Similarly, both of these stations appear to subside, as does station 14, also with decreasing

amplitude moving eastwards ( $\approx -3$  cm at 09 and  $\approx -1$  cm at 08). Station 11 in the north has displacement similar to station 14, but with considerably smaller amplitudes for both components ( $\approx 4$  cm in horizontal and  $\approx -3$  cm in vertical). Even though station 20 apparently seems to preserve a horizontal displacement that is consistent with the stations in the south, its vertical component exhibits a notable amount of subsidence ( $\approx -2$  cm). The latter differentiates its motion from the rest of the stations further to the south, indicating that this part of Cephalonia was also affected by the seismic activity in Paliki.

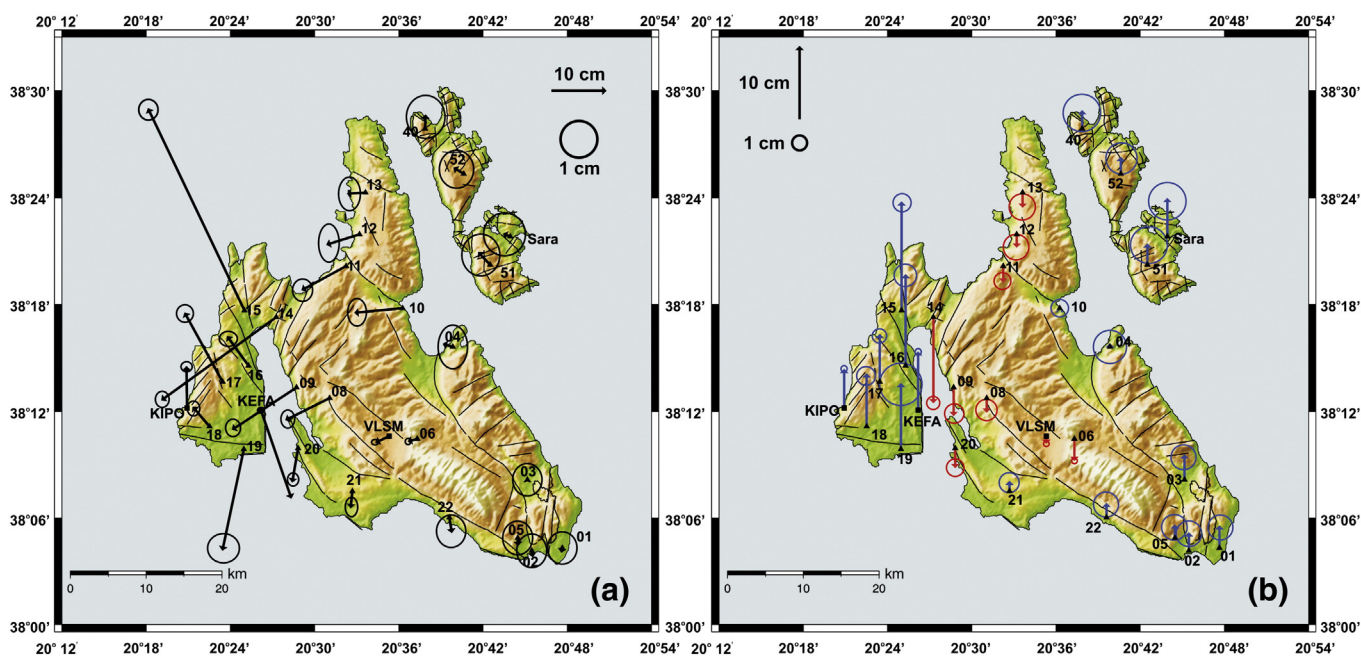


**Fig. 5.** (a) Estimated horizontal, and (b) vertical displacements of Cephalonia–Ithaca GPS Network for the pre-earthquake sequence to 2014 measurement period (time lapse  $\sim 1.2$  months). Red and blue arrows indicate subsidence and uplift, respectively (Reference Frame: IGB08). (For interpretation of the references to colour in this figure legend, the reader is referred to the web version of this article.)

Considering the deformation (amplitude and direction) for the rest of the stations located in the south-eastern and southern part of Cephalonia, it is evident that the area was not considerably affected by the seismic activity in Paliki. The horizontal vectors show an ESE displacement of the area (of about 5–6 cm) which is compatible with the anticipated movement of the region with respect to IGB08 for the time span 2010–2014, whilst the vertical component exhibits a slight uplift (ranging from 1 cm to 3 cm), preserving the pattern of motion of the previous remeasurement period (2007–2010; Lagios et al., 2012). Small deviations that are observed from the consistent pattern outlined above are attributed to local phenomena associated with the complex and extensive nature of faulting in the near proximity.

The observed deformation at the northern stations (12 and 13), as well as at the eastern stations 10 and 04, reveals that this part of the island was also kinematically distressed from the seismic activity in Paliki. The post-seismic activity stretched out to the north and formed a cluster of a large number of low-magnitude events (Fig. 2) which affected the deformation at stations 12 and 13. Moreover, the smaller amplitude of horizontal displacement at station 12 compared to station 13 (1.6 cm and 3.6 cm, respectively), combined with the different horizontal direction between stations 12 and 11, illustrates the critical character of the main NW–SE trending fault zone just to the north of stations 11 and 10, and seems to control the local kinematics of the nearby stations. The latter is more evident at station 10, where a very small deformation is observed (about 0.6 cm in the horizontal and about –1 cm in the vertical) when compared to the anticipated regional movement. This kinematic behaviour highlights the intense stress that occurs in the area close to station 10 (as was pointed out previously by Lagios et al., 2007, 2012) which produces a counterbalance making it to appear as almost stable during the period 2010–2014.

The observed deformations for Ithaca suggest that the island was not strongly affected by the recent seismic activity. A difference in motion between the northern and southern parts is exhibited, where the latter has an eastward displacement with slightly smaller amplitude (about 4 cm) as compared to the former (5–7 cm). Uplift of about 1–3 cm is generally noted. However, station 40 in the north shows an uplift within the error limits (about 3 mm) that is considerably smaller than was measured in previous studies (Lagios et al., 2012). The difference in motion between the northern and southern parts is consistent with the known tectonics of Ithaca which has E–W trending faults that divide it in the middle.

Concerning co-seismic and aftershock deformations (Fig. 5), it is evident that for the affected Paliki area, the same order of magnitude for the horizontal displacement vectors prevails with small changes in direction when compared to prior to the seismic activity (Fig. 4). The most noticeable change in direction is observed only at stations 16 and 19. Additionally, it becomes more obvious that the northern peninsula was affected by the earthquake sequence, since both amplitude and direction of the horizontal component changed considerably. The same is also valid for station 10. However, the stations at the south-eastern part of Cephalonia exhibited almost negligible deformation as expected away from the activated zone. Considering the vertical component (in both Figs. 4b and 5b), the change is quite small and is primarily due to the IGB08 vertical velocity value ( $V_{Up} = 1.3 \pm 1.6$  mm/yr) for the time span of about four years (2010–2014).

### 3. The fault modelling

Forward and inverse modelling was performed to determine the likely causes of the observed ground deformation in Paliki. The models assumed fault activation that runs along Paliki in a NNE–SSW direction. Displacements were quantified using the “*GTdef*” inversion algorithm (Chen et al., 2009; Feng et al., 2012) which implements Okada's (1985) formulation of fault-dislocation.

Horizontal and vertical displacements (together with their error estimates) that describe the co- and part of the post-seismic cumulative

ground deformation for those stations being affected by the earthquake sequence were used as input for the modelling procedure. These stations are located in Paliki, including those about 20 km to the East, together with the stations at the northern peninsula of the island. The most distant stations at the eastern and south-eastern part were not used since negligible deformation was exhibited.

The estimated 2-D geometry of the activated faulting zone was derived based on (i) the GPS deformational vectors, (ii) several iterative attempts of fitting the observed GPS data, and (iii) the constraints inferred by the seismological analysis. The geodetic data from Paliki, having an almost uniform spatial distribution along it, were used to trace the *strike* of the activated zone. The strike was primarily determined by the opposite direction of the horizontal displacements at the Paliki GPS stations (e.g., 14, 19, KEFA, 16, 17, 15). A strike direction of  $24^\circ (\pm 3^\circ)$  CW from North was finally selected. The *length* and the *width* of the zone were initially determined by the areal extent of the post-seismic activity and its distribution along the peninsula (Fig. 2a), as well as the depth distribution of the hypocentres (Fig. 2b). A value of 20 km was assigned for the length of the plane, and a width of 20 km. A trial-and-error iterative procedure was performed to determine an approximate dipping angle for the faulting zone. A dip of  $72^\circ$  to the East was finally determined.

The GPS horizontal components clearly define the right-lateral *slip* character of the fault motion. The vertical components show considerable motion along the dipping side of the faulting zone, which is not however evident from the seismological analysis that indicates a large rake angle (Table 1). Thus, the modelling effort was focused on determining optimal solutions for strike-slip motion along Paliki with a small thrust component. As a consequence, the models were bound to have a right-lateral slip up to –0.50 m (negative sign indicates right lateral slip), and a positive thrust less than 0.2 m (positive sign defines the thrust component). A small tensile component was also allowed, ranging from –0.05 m to +0.05 m. However, the tensile component that was iteratively calculated in the final models was limited to an even smaller range (–0.01 m to +0.01 m), negligibly affecting the modelling results. Moreover, to facilitate the modelling procedure, a small left-lateral and normal component was tolerated up to +0.1 m and –0.05 m, respectively. The selected boundary limits of the slip amplitude were based on the order of the slip that an earthquake of ~M6 can generate (Papazachos and Papazachou, 1997; Wells and Coppersmith, 1994). When allowing a large range of magnitude for slip (up to 2 m) in the modelling procedure, a good fit of the observed data may be achieved, but the resultant mean slip of the fault plane is about 1.4 m and the mean width is limited to ~5 km. However, such values are not supported by earthquakes of magnitude ~M6, as mentioned above. Limiting the slip to the aforementioned values, the width of the fault plane may reach 20 km.

The GPS network in the broader area of Paliki has an average station spacing of about 4–5 km. Therefore, a uniform grid with a patch size of 4 km × 4 km was considered as adequate to resolve the slip distribution along the fault plane. A smoothing factor, *k* (Chen et al., 2009; Feng et al., 2012), was incorporated to constrain the activity of the slip of adjacent patches. This factor defines the motion of each patch and indicates how independent it is as compared to adjacent patches; it essentially describes the roughness of the model (Chen et al., 2009; Feng et al., 2012). It should be noted though that over increasing the smoothing leads to an increase of the misfit between observed and calculated deformation patterns. Therefore, an optimal solution with a realistic slip has to be defined, but at the same time a low misfit needs to be achieved. As such, there is a non-unique solution to describe the deformation.

A checkerboard resolution test for the formed fault-plane models was performed to assess the spatial resolution of the selected GPS stations on resolving the strike-slip and the dip-slip components along it. Alternating values of zero (0) and 1 m of slip were assigned to each of the patches of the 4 km × 4 km grid as synthetic input (Fig. 6a), and

the resulting synthetic displacement at each GPS station was calculated. The estimated errors of the observed GPS vectors were taken into consideration in the inversion. It was found that for a smoothing factor  $k = 100$  the GPS stations recovered almost all the patches to a depth of 16 km, but the resolution decreased for greater depths (Fig. 6b).

### 3.1. Single-fault model

Initially, a *single fault* associated with the activated zone was used to model the observed displacements. This modelled fault (Fig. 7) runs along the eastern part of Paliki with a strike direction of about  $24^\circ$  CW from North. Since no evidence of primary fault ruptures at the surface have been observed (Valkaniotis et al., 2014), the fault (total length of 20 km) was extended from a depth of 20 km to 0.8 km from the ground surface. In addition, an easterly dip angle of  $72^\circ$  from the horizontal was assumed. Its southern edge was set to start near the southern coast of Paliki, where the recorded micro-seismicity constitutes an approximate boundary (Fig. 2). Its northern edge terminates at the northern part of the peninsula. Initially, patches of  $4 \text{ km} \times 4 \text{ km}$  were used to calculate the slip along the plane. However, in order to find a smoother slip distribution, the modelled fault was discretized into a 20 by 20 grid of uniform patches of  $1 \text{ km} \times 1 \text{ km}$  along the strike and dipping directions (Fig. 8).

The burial depth of about  $0.8(\pm 0.2) \text{ km}$  that was adopted in this model was based on the following issues: (i) The lack of evident surface fault exposure in Paliki area, as previously mentioned. (ii) The known seismic velocity model of the upper crust for the broader area, as described in Haslinger et al. (1999), shows that the top surface layer has a width of about 1 km, which is consistent with a boundary at approximately this depth. This top surface layer consists of detrital sediments of variable consolidation (conglomerates, marls, marly limestones and marls with occasional gypsum beds; Lekkas et al., 2001) and exhibits a lower P-velocity (3.5–4.5 km/s) as compared to the underlying layers (Haslinger et al., 1999) which may prevent any likely surface exposure of the rupture. (iii) An outcropping fault of strike-slip character (as is the case in Paliki) would result in horizontal displacements that are significantly different across the strike direction (i.e., tending parallel in opposite directions) as compared to the observed ones (Fig. 5). In

addition, the modelling has shown that a significantly better RMS misfit was obtained by putting the burial depth slightly shallower than 1 km versus the case of an outcropping model.

Inversion models were run using a wide range of smoothing parameters ( $k$ ). The preferred model at  $k = 1500$  had an overall RMS misfit of 0.042 m and was selected due to its position in the inflation corner of the trade-off curve between roughness and misfit (Fig. 7c). The mean right-lateral slip along the entire fault plane was calculated to be 0.35 m, and the mean thrust component was 0.10 m.

Considering Fig. 7a, the overall fit between the observed and calculated horizontal deformational vectors appears to be quite good for almost all stations located on Paliki, but not for stations 14 and 15 regarding their amplitudes. However, the misfit between the observed and calculated vertical components is considerably greater (Fig. 7b), indicating that the modelling was only partially successful by producing the observed sign of motion (i.e. uplift or subsidence) at almost all stations. The calculated spatial horizontal displacements from this modelling attempt (Fig. 8a) emphasizes the strong motion along the eastern part of Paliki and explains the type of the SW motion of the stations located in the rest of Cephalonia (i.e. stations 11, 08, 09).

Considering the movement along the plane, Fig. 8b presents the overall slip that resulted by using the same  $4 \text{ km} \times 4 \text{ km}$  grid as used for the resolution test (Fig. 6) and by assuming a smoothing parameter  $k = 1500$ . It can be seen that the upper part of the rupture plane extends to about 16 km length but becomes longer (reaching 20 km at NE) at greater depths where there is also a good resolution from the checkerboard test. At the upper south-western part of the plane, lower values of slip indicate the termination of the rupture zone, where also the seismicity faints out (Fig. 2). Another upper segment at 8–12 km along the strike (and in the vicinity of station 16, Fig. 7) shows also a small variation of slip as compared to its adjacent parts. It has to be noted that this section of the plane is close to the hypocenter of the second major seismic event ( $M_w = 5.9$ ). Regarding the width of the fault model, the ruptured plane deepens towards the NE, from 13 km to about 18 km at its center, and even more at greater depths ( $>18 \text{ km}$ ) at its north-eastern side. However, the resolution is poorer at its deeper south-western part, as has been shown from the checkerboard test.

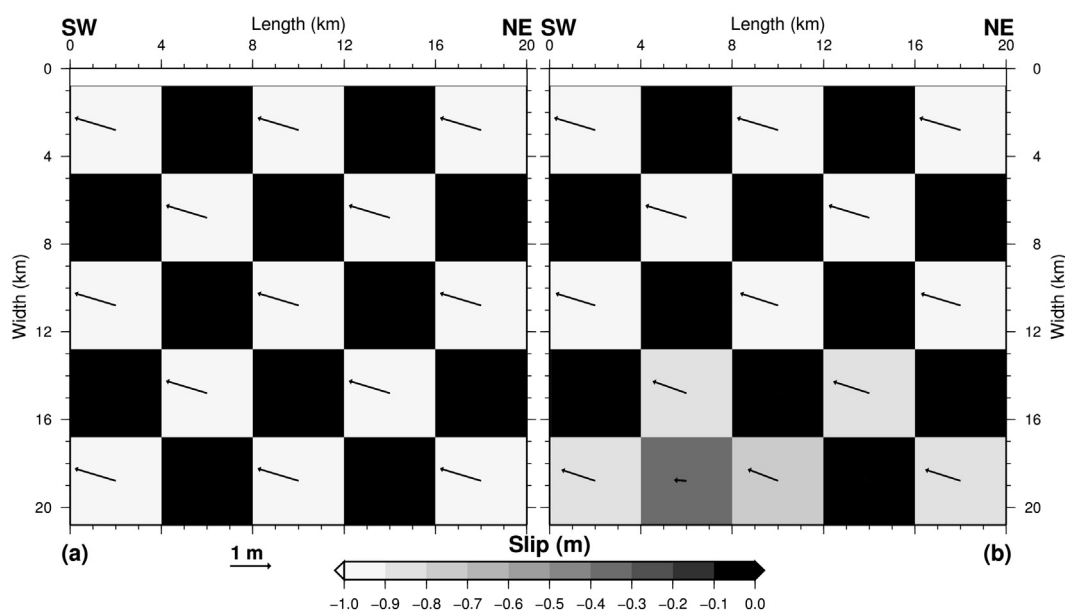


**Fig. 6.** Checkerboard resolution test of the GPS network on the fault plane slip distribution. (a) Synthetic input slip distribution; (b) output best-fit slip distribution at  $k = 100$  inverted from the synthetic surface deformation. Arrows represent the resultant of the dip and slip distribution along the plane. The grey scale indicates only the slip variation. Synthetic fault plane has the same geometric parameters as the *single-fault* model.

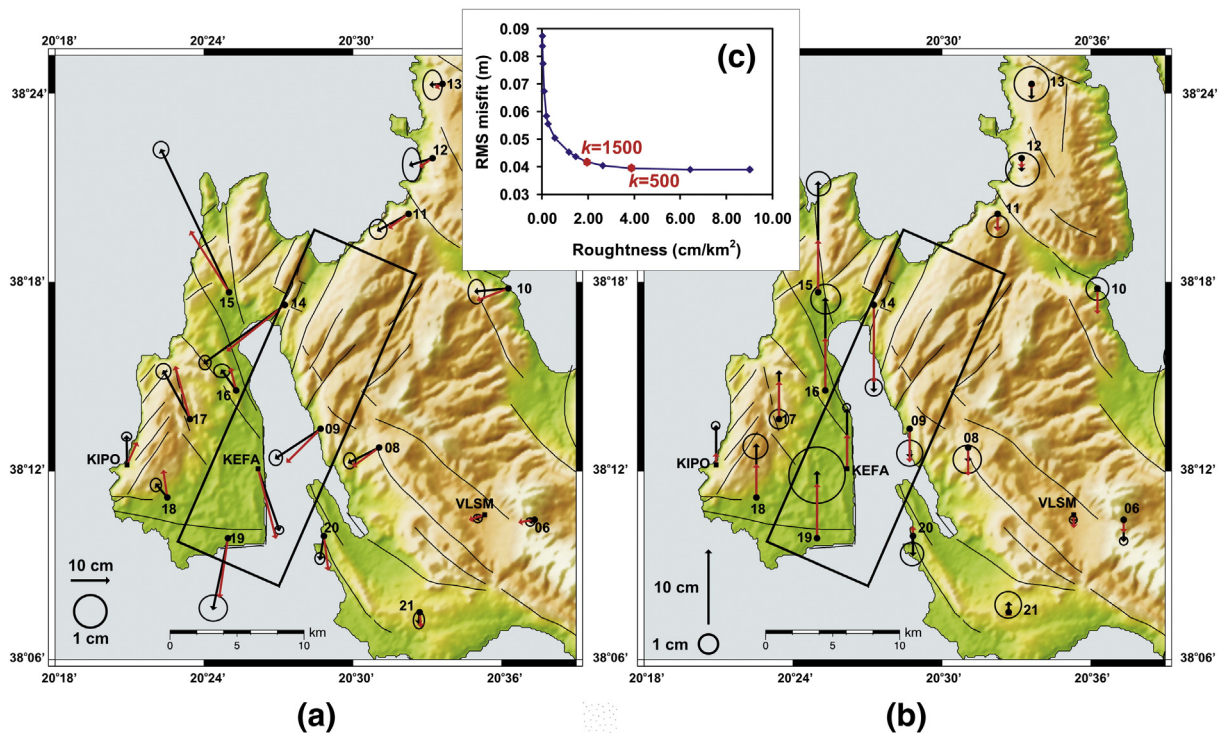


**Fig. 7.** (a) Horizontal, and (b) vertical fitting of the *single-fault* model for  $k = 1500$ . Rectangle indicates the fault plane projected on the ground surface. Black and red arrows indicate the observed and calculated vectors, respectively. (c) The trade-off curve between decreased roughness (increased smoothing) and increased RMS misfit for the *single-fault* model. The preferred model at  $k = 1500$  is chosen at the inflection point of the curve. (For interpretation of the references to colour in this figure legend, the reader is referred to the web version of this article.)

The shape of the rupture plane becomes more apparent when using a denser grid ( $1 \text{ km} \times 1 \text{ km}$ ), as shown in Fig. 8c and d with smoothing parameter of  $k = 500$  and  $k = 1500$ , respectively.

### 3.2. Double-fault model

A second scenario of two different activated faults belonging to the same faulting system is examined in this section. Supporting issues for this scenario emerged from both the seismological and geodetic data: (i) the different focal depths of the two major events, (ii) the different dipping angles ( $70^\circ$  and  $62^\circ$ ) of their planes, (iii) the different location of the hypocenter of the second major event that shifted to the NW at a shallower depth (Table 1), and (iv) the geodetic data that notably exhibit greater amplitudes of deformation for GPS stations located at the northern part of Paliki (stations 14, 15), together with a rotation of the horizontal vector compared to the vectors at the southern stations (Fig. 5). Additionally, the slight slip “discontinuity” at the upper part of the plane that is close to the second major hypocentral event, as previously pointed out in the *single-fault* model (Fig. 8b), may indicate a local kinematic complexity as illustrated by the “strange” behaviour of station 16. The motion observed at this station is considerably smaller from the anticipated motion, especially when it is compared to the deformation measured in the nearby stations 14, 17 and KEFA. This difference implies that the observed vector was probably affected by a reverse motion of a nearby fault that may be associated with the second major seismic event ( $M_w = 5.9$ ). Also, the occurrence of the  $M_w = 5.2$  in that area (Fig. 2) is consistent with tectonic complexity.

Applying the same procedure for the resolution test as in the *single-fault* model, the planes of the two faults were discretized into uniform patches of  $4 \text{ km} \times 4 \text{ km}$  and  $3.3 \text{ km} \times 3.3 \text{ km}$  for the southern and northern faults, respectively (Supplementary Section). It was similarly found as in the *single-fault* model that good resolution was achieved for depths up to 12 km but with a decreasing resolution at greater depths.

The southern (AB) modelled fault (Fig. 9) was set to run along the southern part of Paliki, on a strike direction of about  $24^\circ$  CW from North. The strike direction, dipping angle and locking depth of this fault were similarly determined as in the *single-fault* model verifying the seismological parameters of the first major event ( $M_w = 6.1$ ), as well as the  $M_w = 5.2$  event (Table 1). It extends from a locking depth of 20 km to a burial depth of  $0.8 (\pm 0.2) \text{ km}$ , dipping to the East at an angle of  $72^\circ$  from the horizontal, and having a total length of 12 km which terminates to the NE of station 16. The fault plane (Fig. 10a) was initially discretized into  $4 \text{ km} \times 4 \text{ km}$  patches, and also into a grid of  $1 \text{ km} \times 1 \text{ km}$  for a smoother representation of the slip’s distribution (Fig. 10b).

The location of the northern (CD) modelled fault (also discretized into  $3.3 \text{ km} \times 3.3 \text{ km}$ , and  $1 \text{ km} \times 1 \text{ km}$ ) was considered on the basis of the issues outlined above, as well as the fitting results from various modelling attempts. The southern end of this fault was located NW of station 16. Its strike direction was set to  $28^\circ$  CW from North, and its length to 10 km. A shallower burial depth of about  $0.5 (\pm 0.1) \text{ km}$  and a locking depth of 18 km were finally determined, which is consistent to the small focal depth (5 km) of the second major seismic event, as well as with the plethora of surface ruptures in that area (Lekkas et al., 2014; Valkaniotis et al., 2014). The best fit was obtained by setting the fault plane to dip eastwards at  $65^\circ$  from the horizontal.

The fit between observed and calculated displacement vectors appears to be very good concerning the horizontal component (Fig. 9a), and relatively good for the vertical component (Fig. 9b). The spatial ground deformation (Fig. 9c) is similar to the first case scenario. The preferred  $k$  factor for this *double-fault* model was also 1500 (Fig. 9d) yielding an overall RMS misfit of 0.037 m, which is an improvement compared to the *single-fault* model. Consequently, the fit improved with respect to the *single-fault* scenario, especially at stations 14 and 15, an area associated with the northern modelled fault. A mean right-lateral slip of 0.34 m and 0.29 m, together with a mean dip-thrust

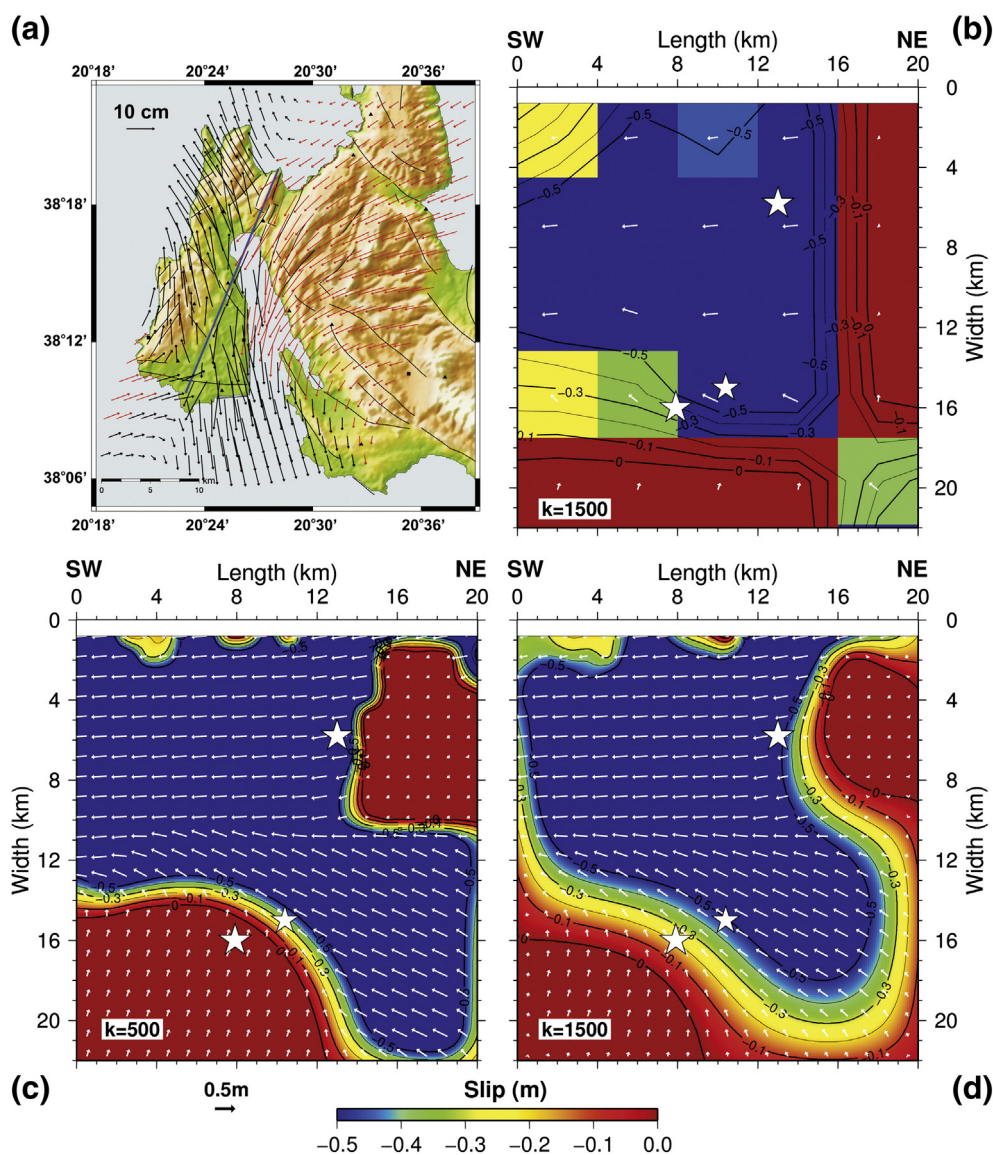


**Fig. 8.** (a) Horizontal spatial deformation for the *single-fault* model (blue line). Red and black arrows indicate areas where *qualitative* subsidence and uplift take place. (b) Slip distribution on the plane of the *single-fault* model discretized at  $4 \text{ km} \times 4 \text{ km}$  patches for  $k = 1500$ . (c), (d) Slip distribution on the plane of the *single-fault* model discretized at  $1 \text{ km} \times 1 \text{ km}$  patches for  $k = 500$ , and  $k = 1500$ , respectively, as shown in Fig. 7c. Arrows represent the resultant of the dip and slip distribution along the plane. The coloured scale indicates only the slip variation. White stars represent the horizontal projection on the plane of the three seismic events. (For interpretation of the references to colour in this figure legend, the reader is referred to the web version of this article.)

component of 0.07 m and 0.09 m was calculated for the southern and northern faults, respectively.

Looking at the slip distribution (Fig. 10) for both fault planes, the southern one (AB) shows a rather uniform pattern with relatively high slip values ( $\sim 0.5 \text{ m}$ ) except at its south-western upper part where smaller values are observed (Fig. 10a); this pattern also appears in the *single-fault* model (Fig. 8b). The depth of the rupture extends to approximately 16–18 km. However, the northern fault (CD) shows more distinctive features. The lower part of the plane ( $> 12 \text{ km}$ ) shows a significant right-lateral thrust motion, indicating a pattern which can also be seen in the lower north-eastern part of the *single-fault* model (Fig. 8d). At shallower depths (8–12 km), there is a narrow section of lower slip ( $\sim 0.35 \text{ m}$ ) overlaid by a layer of higher slip ( $\sim 0.5 \text{ m}$ ). It is worth mentioning that this upper segment at the south-western part of the CD fault encompasses the hypocenter of the second major event ( $M_w = 5.9$ ), indicating probably that the occurrence of this rupture extended to shallower depths. The other high-slip segment at the upper north-eastern part may be associated with the effect observed

at the three (3) northern GPS stations from the off-shore post-seismic sequence (Fig. 2). All the above described characteristics are shown better in a smoother manner, and particularly for the grid of  $1 \text{ km} \times 1 \text{ km}$  (Fig. 10b) that was implemented for this purpose.

Finally, the case of the *double-fault* model was examined for greater burial depths in an attempt to assess the aftershock component that is inherent in the GPS data. It was found that the overall fit between observed and calculated data significantly deteriorates for burial depths greater than 1.8 km and 1.3 km for the southern and northern faults, respectively (Supplementary Section). The modelled horizontal and vertical vectors of ground deformation at most of the stations located in Paliki significantly decreased. However, the fit remained fairly good for those stations to the east of Paliki where limestones generally prevail. This indicates that a considerable aftershock component is inherent in the observed deformation at Paliki. The fault planes of the two faults show uniform but intense ( $> 0.6 \text{ m}$ ) and extensive slip along their surface planes. The rupture plane of the southern fault extends to a depth of almost 24 km, while the second fault extends to more than 18 km.

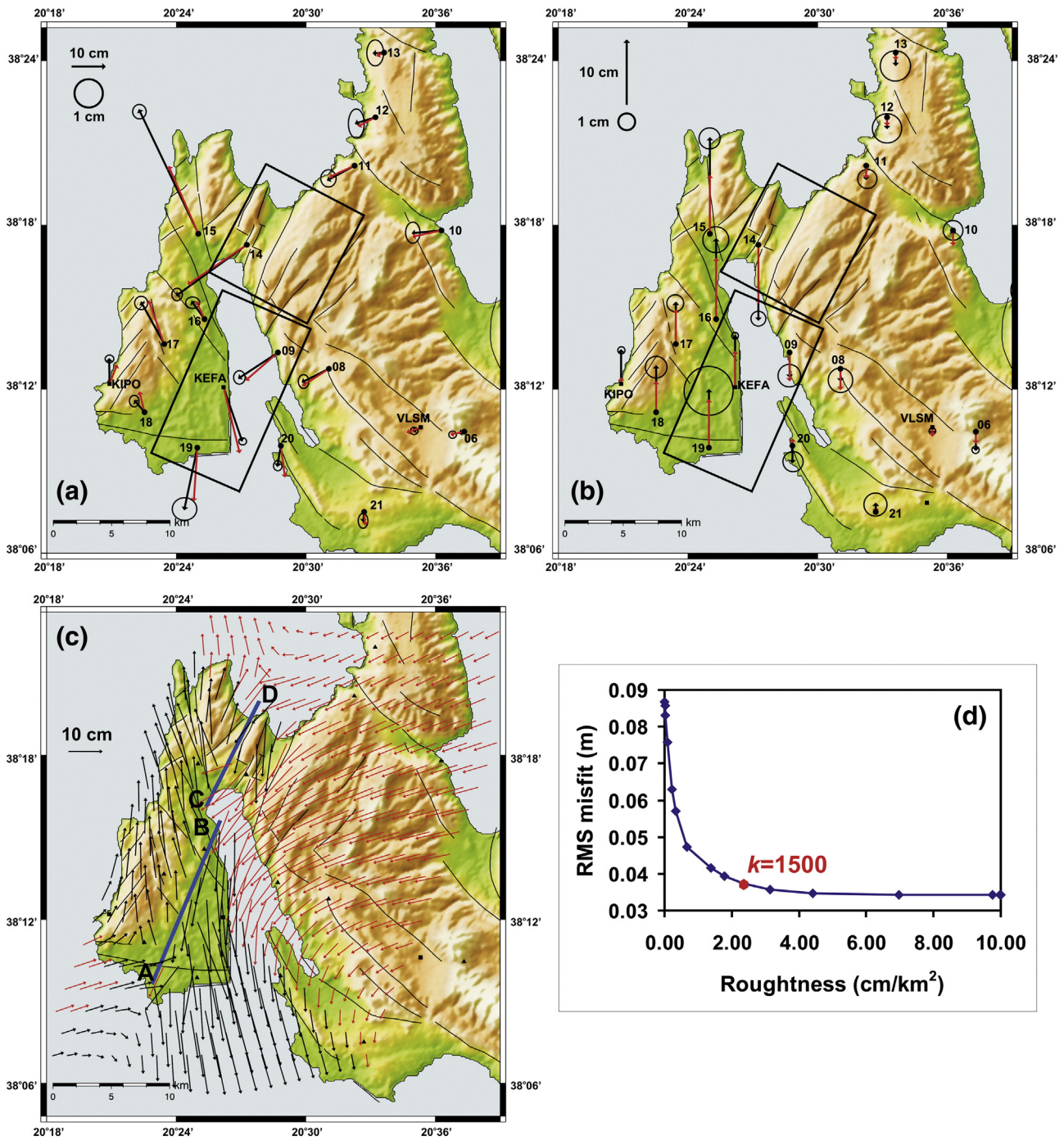


**Fig. 9.** (a) Horizontal, and (b) vertical fitting for the *double-fault* model at burial depths of 0.8 km and 0.5 km for the southern and northern faults, respectively, for  $k = 1500$ . Rectangles indicate the fault planes of the two faults (with different dipping angles) projected on the ground surface. Black and red arrows indicate the observed and calculated vectors, respectively. (c) Horizontal spatial deformation for the *double-fault* model (blue line). Red and black arrows indicate areas where *qualitative* subsidence and uplift take place. (d) The trade-off curve between decreased roughness (increased smoothing) and increased RMS misfit for *double-fault* model. The preferred model at  $k = 1500$  is chosen balancing the trade-off between misfit and smoothing. (For interpretation of the references to colour in this figure legend, the reader is referred to the web version of this article.)

The former indicates that the modelling procedure (in order to fit the observed data) increases the area of rupture and the amplitude of slip as the burial depth increases. It is noted that the resultant burial depths (1.8 km and 1.3 km) were found to be the maximum depths with a relatively acceptable fit between observed and calculated data (RMS misfit 0.063 m). Greater burial depths resulted in either large RMS errors (>0.09 m), inevitably leading to large misfits, or large amplitudes of slip and fault dimensions which are not justified and are not consistent with earthquakes of magnitudes  $\sim M6$  (Wells and Coppersmith, 1994).

#### 4. Discussion–conclusions

Processing and interpretation of local GPS data from the Cephalonia-Ithaca network, which were collected in early 2014, have clearly identified the significant ground deformation that occurred in the area and have made possible the characterization of the seismogenic faults that generated the intense seismic activity. GPS results from previous re-measuring periods (2001–2010) revealed reliably small velocity values of ground deformation (on the order of mm/yr) in both horizontal and

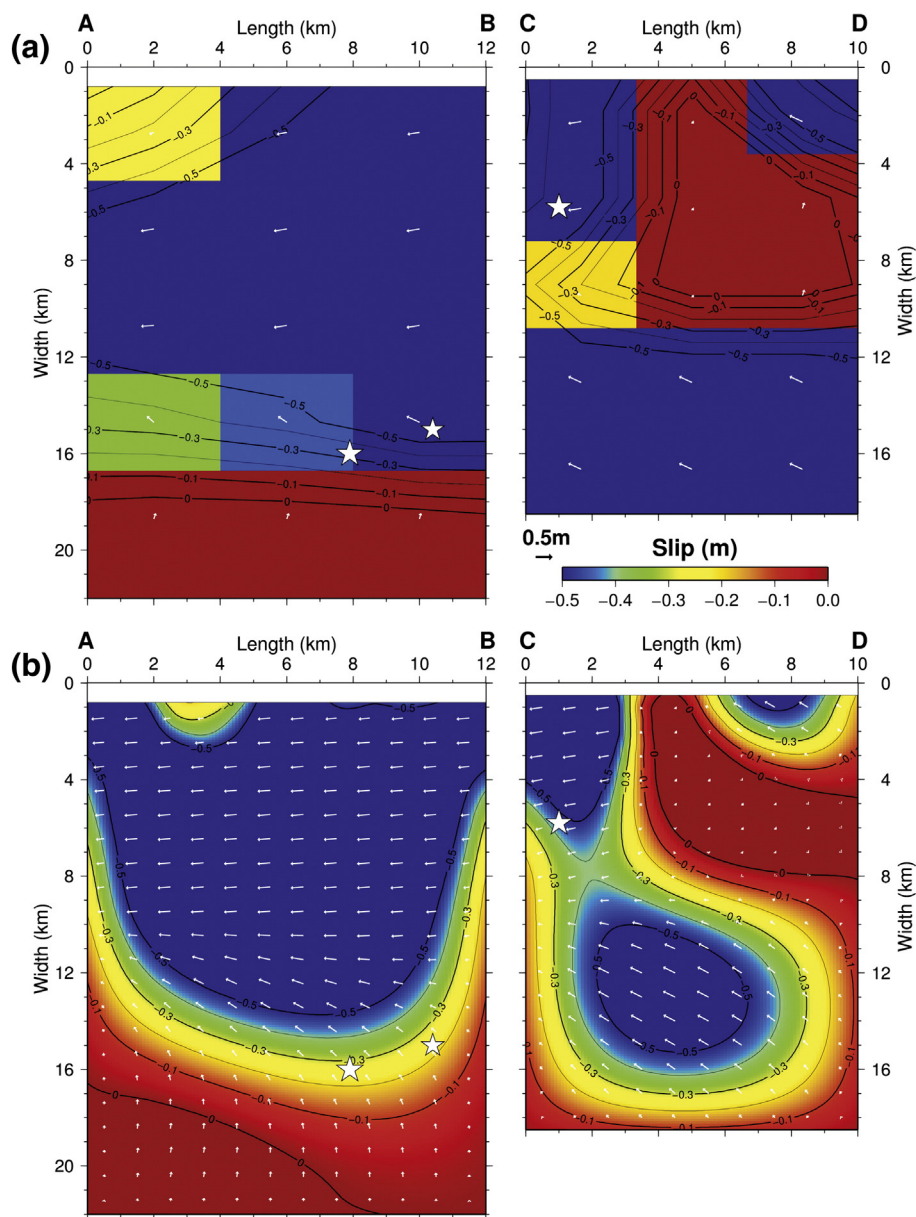


**Fig. 10.** (a) Slip distribution on the planes of the *double-fault* model discretized at 4 km × 4 km and 3.3 km × 3.3 km patches for the southern (AB) and northern (CD) faults, respectively, for  $k = 1500$ . (b) Slip distribution on the planes of the *double-fault* model discretized at 1 km × 1 km patches for  $k = 1500$ . Arrows represent the resultant of the dip and slip distribution along the planes. The coloured scale indicates only the slip variation. White stars represent the horizontal projection on the plane of the three seismic events. (For interpretation of the references to colour in this figure legend, the reader is referred to the web version of this article.)

vertical components (Lagios et al., 2007, 2012). These long-term data were used to correct the four-year motion (2010–2014) and to estimate the GPS coordinates prior to the occurrence of the earthquake sequence. With these corrections, the co-seismic and the likely aftershock deformations were modelled.

The strongest deformation was recorded at stations at Paliki where the earthquakes' epicenters were located. The seismological results relating to focal mechanism of these seismic events cannot distinguish between the two auxiliary planes (Fig. 2). Those earthquakes can be either right-lateral strike-slip events on a NE–SW plane or left-lateral strike-slip events on a NW–SE plane. The present study provided a definitive answer to the ambiguity. Specifically, the horizontal trajectories of the GPS data clearly indicate a right-lateral character of faulting (Figs. 4, 5). However, the relatively large vertical uplift observed at all stations on Paliki cannot be explained from seismological analysis. Vertical differential motion along the peninsula, decreasing from east to west, is the only indicator of a thrust component that can match the results

of the earthquake focal mechanisms. The strange behaviour of some stations in Paliki (stations 15, 16) is attributed to local tectonic motions and geological characteristics. The motion of station 16, located almost above the hypocenter of the  $M_w = 5.2$  event, might have been the result of complex exerted forces. That would explain the most extensive damages, together with observed ground cracks and fissures, which were reported in the area between stations 15 and 16.

Stations adjacent to and to the east of Paliki had relatively smaller amplitudes of ground deformation that were modelled very well. Moreover, the absence of any significant structural damages to the east of Paliki implies that a possible kinematic boundary may exist between Paliki and the main part of Cephalonia (in the marine area) which obstructed the eastward release of seismic energy. This conjecture is also supported by the fact that post-seismic activity has been confined to Paliki (Fig. 2). Results from the stations located at the southern and eastern parts of the island, together with those on Ithaca, have shown displacements that are consistent with the expected regional motion

with respect to IGB08 during the four years 2010–2014 (Fig. 4). Thus, these areas were not affected by the seismic activity that had occurred to the west.

Modelling procedures were performed to define the source parameters of the activated faults that generated the seismic sequence in Cephalonia. A number of possible scenarios were considered but only two models were finally selected as the most plausible ones. Lack of GPS observations between the two major events forced us to consider a *single-fault*, model which treats the whole seismic sequence as a single modelling event. However, based on the modelling results of the *single-fault* approach, together with the different characteristics of the two major events, a more tectonically realistic concept of the *double-fault* model was introduced. For this model, each major event may be associated with a different fault but belonging to the same faulting system.

The *single-fault* model provided a reasonably good fit with small RMS misfit between observed and calculated geodetic data. This single fault extends along the total length of the eastern part of Paliki (about 20 km), where most of the post-seismic activity was concentrated (Fig. 2). The parameters of the focal mechanism for the first major event ( $M_w = 6.1$ ) are consistent with the geometry of the fault plane (azimuth and dip angles); however, there is a larger deviation between the fault parameters and those of the focal mechanism for the second major event ( $M_w = 5.9$ ) as summarized in Table 1.

The *double-fault* model (Fig. 9) resulted in the best RMS misfit and is the preferred model to explain the observed ground deformation and seismological results. The two faults are offset to the NW and are part of the same NE–SW trending fault zone but have different characteristics. The southern fault is longer and is associated with the occurrence of the first two seismic events ( $M_w = 6.1$  &  $M_w = 5.2$ ) that had similar focal depths. The northern one is shorter and is associated with the shallowest event ( $M_w = 5.9$ ). The shorter width and shallower position of the northern fault may explain the shallowing character of the aftershock activity that is illustrated in Fig. 2b. It is worth mentioning that most of the structural damage and ground fractures were reported in the broader area between the offset of the two faults. The modelled burial depths of  $0.8(\pm 0.2)$  km and  $0.5(\pm 0.1)$  km for the two faults are consistent with the lack of major undisputed outcropping fault traces in the area of Paliki during the earthquake sequence.

The modelled fault activation for the above scenarios does not fully account for all of the observed ground deformation, and especially the vertical component. Efforts to effectively model the vertical component were not particularly successful, or resulted in non-realistic scenarios (i.e. strong dipping component). The fault characteristics that are needed to fit the observed vertical deformation in Paliki adversely affect the areal extent of the faults and mainly the slip vector of the two faults. The modelling indicates that most probably a small normal component should exist on the slip vector, at least for depths of less than 8 km. Such a component, though, is not consistent with the seismological analysis. Moreover, efforts to eliminate the small “normal-fault” component being presented in the patches closer to the surface, resulted in even greater misfits between predicted and observed ground deformation. Therefore, the existence of a small amplitude “normal-fault” component should rather be considered in the upper part of the activated faults in order to account for the observed vertical deformation. However, since the vertical component of GPS data is also affected by non-tectonic sources, efforts to fit the observed vertical displacements were primarily concentrated on *truly* fitting spatially the direction of motion (i.e. uplift or subsidence as depicted in Figs. 8a and 9c), and then their amplitudes.

Post-seismic activity has also to be considered in order to explain the greater amplitudes of horizontal deformation that were observed at some stations (e.g. stations 14 & 15), where the adopted models were unsuccessful when applying realistic constraints (i.e. slip amplitude). Additionally, the occurrence of a very large number of earthquakes (more than 600 events of  $2.5 < M_w < 3.5$  between the two major events) in such a highly fractured environment suggests that some kind of motion along small local faults might have taken place.

Lack of observations between the two major events makes it impossible to determine the contribution of each event to the observed ground deformation. The predicted horizontal displacement of each fault relative to the motion of the cGPS VLSM station (located on Alpine limestone basement away from the activated zone) after the two main events revealed that the southern fault associated with the  $M_w = 6.1$  &  $M_w = 5.2$  events contributed to an almost 70% of the overall modelled displacement (Fig. 4c). The rest of the modelled displacement is from the northern fault which is associated with the  $M_w = 5.9$  event. In any case the total modelled vector of the horizontal displacement (44 mm) is greater than the observed one (28 mm; Fig. 9a). Similarly, the largest contribution to the vertical component is attributed to the southern fault (~11 mm), while ~4 mm is attributed to the northern fault. These values (~15 mm of subsidence in total) are also greater than the observed one (~12 mm; Fig. 9b). It is therefore evident that these discrepancies should be attributed to a post-seismic component which is inherent in the data for stations mainly located at the northern part of Paliki, which were used for modelling, and were reflected on the slip characteristics of the two modelled faults. The latter has also been demonstrated when implementing greater burial depths (>1.8 km) for the fault planes, and a good fit resulted for the stations to the east of Paliki. The significant amplitude of the post-seismic component in the northern highly fractured and tectonically complicated part of Paliki is attributed to: (i) the young sediments on which the GPS stations are installed and, (ii) the intense aftershock activity prior to the measurements of the last campaign.

As a final point, it is worth mentioning the previously published works relating to ground deformation and tectonic regime of the broader area. Combined analysis of GPS and Permanent Scatterer Interferometric data for the period 2003–2010 has shown that an intense non-linear uplift took place at Paliki and along the major NW–SE trending thrusting zone at the southern part of Cephalonia when compared to the previous decade (Lagios et al., 2012). The same non-linear uplift also took place at the northern part of Zakynthos Island (just south of Cephalonia), based on PSI analysis for the same comparative periods (Sakkas et al., 2014). This differentiation of the deformational pattern for these two periods was interpreted as a possible regional dilatancy (Lagios et al., 2012) which potentially could lead to strong seismic events. The two earthquakes of January ( $M_w = 6.1$ ) and February ( $M_w = 5.9$ ) of 2014 that occurred in the western part of Cephalonia (Paliki), where the maximum increasing rate of non-linear uplift was observed, confirmed that interpretation.

## Acknowledgements

The authors would like to thank Dr. L. Feng and an anonymous reviewer for their constructive comments, together with Professors P. Papadimitriou and A. Tzanis (Department of Geophysics & Geothermics, University of Athens, Greece) for useful discussions, and Dr. B. Damiata (UCLA) for proofreading the manuscript. Continuous GPS data from stations VLSM and KIPO were provided by the Geodynamic Institute of the National Observatory of Athens, Greece. Figures were made using the Generic Mapping Tool Software (Wessel and Smith, 1998).

## Appendix A. Supplementary data

Supplementary data to this article can be found online at <http://dx.doi.org/10.1016/j.tecto.2015.01.010>.

## References

- Chen, T., Newman, A.V., Feng, L., Fritz, H.M., 2009. Slip distribution from the 1 April 2007 Solomon Islands earthquake: a unique image of near-trench rupture. *Geophys. Res. Lett.* 36, L16307. <http://dx.doi.org/10.1029/2009GL039496>.
- Dach, R., Hugentobler, U., Fridez, P., Meindl, M., 2007. *Bernese GPS Software Version 5.0*. Astronomical Institute, University of Bern, Bern.

- Feng, L., Newman, A.V., Protti, M., González, V., Jiang, Y., Dixon, T.H., 2012. Active deformation near the Nicoya Peninsula, northwestern Costa Rica, between 1996 and 2010: interseismic megathrust coupling. *J. Geophys. Res.* 117, B06407. <http://dx.doi.org/10.1029/2012JB009230>.
- Galanopoulos, A., 1962. Monographie, Institut Géographique National. *Int. Union Geodesy Geophys.* 18, 15.
- Ganas, A., Marinou, A., Anastasiou, D., Paradissis, D., Papazissi, K., Tzavaras, P., Drakatos, G., 2013. GPS-derived estimates of crustal deformation in the central and north Ionian Sea, Greece: 3-yr results from NOANET continuous network data. *J. Geodyn.* 67, 62–71.
- Haslinger, F., Kissling, E., Ansoerge, J., Hatzfeld, D., Papadimitriou, E., Karakostas, V., Makropoulos, K., Kahle, H.G., Peter, Y., 1999. 3-D crustal structure from local earthquake tomography around the Gulf of Arta (Ionian region, NW Greece). *Tectonophysics* 304, 201–218.
- Hollenstein, Ch., Müller, M.D., Geiger, A., Kahle, H.-G., 2008. Crustal motion and deformation in Greece from a decade of GPS measurements 1993–2003. *Tectonophysics* 449, 17–40.
- Karakostas, V., Papadimitriou, E., Mesimeri, M., Gkarlaouni, C., Paradisopoulou, P., 2014. The 2014 Kefalonia Doublet (Mw 6.1 and Mw 6.0), Central Ionian Islands, Greece: seismotectonic implications along the Kefalonia Transform Fault Zone. *Acta Geophys.* <http://dx.doi.org/10.2478/s11600-014-0227-4>.
- Lagios, E., Papadimitriou, P., Novali, F., Sakkas, V., Fumagalli, F., Vlachou, K., Del Conte, S., 2012. Combined seismicity pattern analysis, DGPS and PSInSAR studies in the broader area of Cephalonia (Greece). *Tectonophysics* 524–525, 43–58.
- Lagios, E., Sakkas, V., Papadimitriou, P., Damiata, B.N., Parcharidis, I., Chousianitis, K., Vassilopoulou, S., 2007. Crustal deformation in the Central Ionian Islands (Greece): results from DGPS and DInSAR analyses (1995–2006). *Tectonophysics* 444, 119–145.
- Lekkas, E., Danamos, G., Mavrikas, G., 2001. Geological structure and evolution of Kefallonia and Ithaki Islands. *Bull. Geol. Soc. Greece XXXIV/1*, 11–17.
- Lekkas, E., Mavroulis, S., Alexoudi, V., 2014. The geodynamic and seismotectonic setting of Cephalonia (Ionian Sea, Western Greece) as factor controlling the distribution of earthquake environmental effects and structural damage induced by early 2014 earthquakes (January 26th and February 3rd, Mw 6.0). *International Workshop on Seismic Hazard and Earthquake Engineering*. Abstract. Technological Educational Institute of Ionian Islands.
- Louvari, E., Kiratzi, A., Papazachos, B.C., 1999. The Cephalonia Transform Fault and its extension to western Lefkada Island (Greece). *Tectonophysics* 308, 223–236.
- Okada, Y., 1985. Surface deformation due to shear and tensile faults in a half-space. *Bull. Seismol. Soc. Am.* 75 (4), 1135–1154.
- Papadimitriou, P., Voulgaris, N., Kouskouna, V., Kassaras, I., Kaviris, G., Pavlou, K., Karakonstantis, A., Bozionelos, G., Kapetanidis, V., 2014. The Kefallinia Island earthquake sequence January – February 2014. Abstract, 2nd ECEES, Istanbul, Turkey.
- Papadimitriou, P., Chousianitis, K., Agalos, A., Moshou, A., Lagios, E., Makropoulos, K., 2012. The spatially extended 2006 April Zakynthos (Ionian Islands, Greece) seismic sequence and evidence for stress transfer. *Geophys. J. Int.* 190 (2), 1025–1040.
- Papadimitriou, P., Kaviris, G., Makropoulos, K., 2006. The Mw=6.3 2003 Lefkada Earthquake (Greece) and induced stress transfer changes. *Tectonophysics* 423, 73–82.
- Papadopoulos, G., Karastathis, V.K., Koukouvelas, I., Sachpazi, M., Baskoutas, I., Chouliaras, G., Agalos, A., Daskalaki, E., Minadakis, G., Moshou, A., Spanos, D., Triantafyllou, I., 2014. The Cephalonia, Ionian Sea (Greece), sequence of strong earthquakes of January–February 2014: a first report. *Res. Geophys.* <http://dx.doi.org/10.4081/rg.2014.5441>.
- Papazachos, B., Papazachou, C., 1997. *The Earthquakes of Greece*. Ziti, Thessaloniki, Greece.
- Pavlidis, S., Papadopoulos, G.A., Ganas, A., Papathanasiou, G., Karastathis, V., Keramydas, D., Fokaefs, A., 2004. The 14 August 2003 Lefkada (Ionian Sea) earthquake. *Proceedings of the 5th Int. Symp. on Eastern Med. Geology* 2, 942–946. Thessaloniki 14–20 April, Greece.
- Protti, M., González, V., Newman, A.V., Dixon, T.H., Schwartz, S.Y., Marshall, J.S., Feng, L., Walter, J.L., Malservisi, R., Owen, S.E., 2014. Nicoya earthquake rupture anticipated by geodetic measurement of the locked plate interface. *Nat. Geosci.* 7, 117–121.
- Reilinger, R., McClusky, S., Paradissis, D., Ergintav, S., Vernant, P., 2010. Geodetic constraints on the tectonic evolution of the Aegean region and strain accumulation along the Hellenic subduction zone. *Tectonophysics* 488 (1–4), 22–30.
- Sakkas, V., Novali, F., Lagios, E., Vassilopoulou, S., Damiata, B.N., Fumagalli, A., 2014. Ground deformation of Zakynthos Island (Western Greece) observed by PSI and DGPS. *Geosciences and Remote Sensing Symposium (IGARSS), 2014 IEEE International, Quebec Canada*, pp. 4792–4795.
- Stiros, S.C., Pirazzoli, P.A., Laborel, J., Laborel-Deguen, F., 1994. The 1953 earthquake in Cephalonia (Western Hellenic Arc): coastal uplift and halotectonic faulting. *Geophys. J. Int.* 117, 835–849.
- Valkaniotis, S., Ganas, A., Papathanassiou, G., Papanikolaou, M., 2014. Field observations of geological effects triggered by the January–February 2014 Cephalonia (Ionian Sea, Greece) earthquakes. *Tectonophysics* 630, 150–157.
- Wells, D.L., Coppersmith, J.K., 1994. New empirical relationships among magnitude, rupture length, rupture width, rupture area, and surface displacement. *Bull. Seismol. Soc. Am.* 84, 974–1002.
- Wessel, P., Smith, W.H.F., 1998. New, improved version of Generic Mapping Tools released. *EOS Trans. Am. Geophys. Union* 79, 579.